Journal Pre-proof

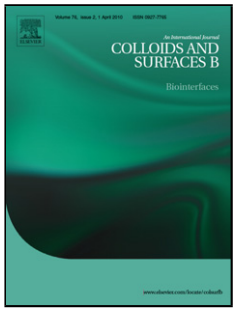

Cell adhesion in microchannel multiple constrictions – evidence of mass transport limitations

S.F. Neves (Methodology) (Investigation)<ce:contributor-role>Writing –original draft) (Writing - review and editing) (Software) (Data curation) (Visualization), J. Ponmozhi (Investigation)<ce:contributor-role>Writing –original draft) (Data curation), F.J. Mergulhão (Conceptualization) (Resources) (Writing - review and editing) (Methodology) (Supervision) (Funding acquisition), J.B.L.M. Campos (Resources) (Writing - review and editing) (Supervision) (Project administration) (Funding acquisition), J.M. Miranda (Conceptualization) (Methodology) (Software) (Visualization)<ce:contributor-role>Writing –original draft) (Writing - review and editing) (Supervision) (Project administration) (Funding acquisition)

PII: S0927-7765(20)30846-8

DOI: https://doi.org/10.1016/j.colsurfb.2020.111490

Reference: COLSUB 111490

To appear in: *Colloids and Surfaces B: Biointerfaces*

Received Date: 18 August 2020

Revised Date: 30 October 2020

Accepted Date: 20 November 2020

Please cite this article as: Neves SF, Ponmozhi J, Mergulhão FJ, Campos JBLM, Miranda JM, Cell adhesion in microchannel multiple constrictions – evidence of mass transport limitations, *Colloids and Surfaces B: Biointerfaces* (2020), doi: https://doi.org/10.1016/j.colsurfb.2020.111490

Cell adhesion in microchannel multiple constrictions – evidence of mass transport limitations

S. F. Neves[1], J. Ponmozhi[1,2], F. J. Mergulhão[3], J. B. L. M. Campos[1], J. M. Miranda[1*]

[1] CEFT - Transport Phenomena Research Center, Department of Chemical Engineering, Faculty of Engineering, University of Porto, Rua Dr. Roberto Frias s/n, 4200-465 Porto, Portugal

[2] IES- Institute of Engineering & Science IPS Academy Knowledge Village, Rajendra Nagar A.B. Road, Indore-452012, India

[3] LEPABE - Laboratory for Process Engineering, Environment, Biotechnology and Energy, Faculty of Engineering, University of Porto, Rua Dr. Roberto Frias, 4200-465 Porto, Portugal

*Corresponding author. Email: jmiranda@fe.up.pt

Graphical abstract

Annexes' Files

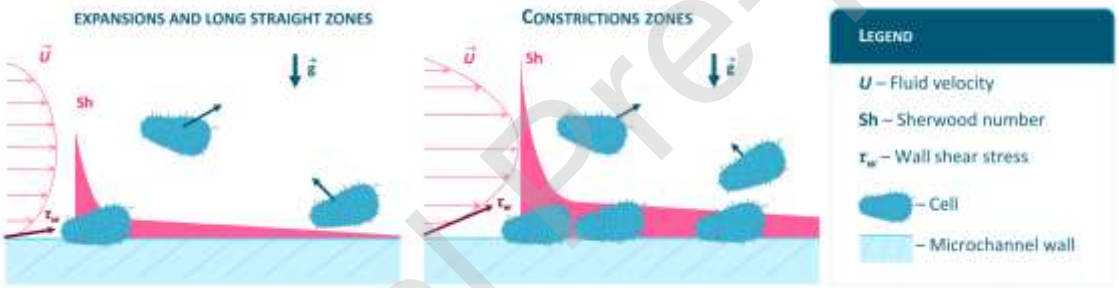

Highlights

- Experimental cell adhesion test conducted in a multiple constrictions microchannel
- Unexpected increase of cells adhesion in regions with high local wall shear stress
- For this flow regime, mass transport limitation were numerically assessed
- The numerical and experimental data of cell adhesion showed similar tendency
- Correlation between adhered cells and local Sherwood distribution was obtained

Abstract

Biofilm growth (fouling) in microdevices is a critical concern in several industrial, engineering and health applications, particularly in novel high-performance microdevices often designed with complex geometries, narrow regions and multiple headers. Unfortunately, on these devices, the regions with local high wall shear stresses (WSS) also show high local fouling rates. Several explanations have been put forward by the scientific community, including the effect of cell transport by Brownian motion on the adhesion rate. In this work, for the first time, both WSS and convection and Brownian diffusion effects on cell adhesion were evaluated along a microchannel with intercalate constriction and expansion zones designed to mimic the hydrodynamics of the human body and biomedical devices. Convection and Brownian diffusion effects were numerically studied using a steady-state convective-diffusion model (convection, diffusion and sedimentation). According to the numerical results, the convection and Brownian diffusion effects on cell adhesion are effectively more significant in regions with high WSS. Furthermore, a good agreement was observed between experimental and predicted local Sherwood numbers, particularly at the entrance and within the multiple constrictions. However, further mechanisms should be considered to accurately predict cell adhesion in the expansion zones. The described numerical approach can be used as a way to identify possible clogging zones in microchannels, and defining solutions, even before the construction of the prototype.

Keywords: Localized biofouling; Wall shear stress; Sherwood number; adhesion rate distribution; biomedical applications; numerical simulations

Notation

u	Velocity	m/s
p	Pressure	Pa
C	Cells concentration	$kg{\cdot}m^{-3}$

D_f	Brownian diffusivity of cells in water	$m^2 \cdot s^{-1}$
h	Height of the channel	m
k_m	Coefficient of convective mass transfer	m/s
n_∞	Number of cells at the inlet	$cells \cdot m^{-3}$
A	Area	m^2
Q	Flow rate	m^3/s
J_{cell}	Cell flux	$kg \cdot m^{-2} \cdot s^{-1}$
N_B	Total cells adhered	cells
L_w	Length of the wide section of the multiple constriction section	m
L_c	Length of the constriction	m
L_{in}	Length of the inlet section	m
L_{out}	Length of the outlet section	m
Re	Reynolds number	-
Sh	Sherwood number	-
V	Volume	m^3
W	Width of the channel	m
W_c	Width of the constriction	m
Δt	Adhesion time	s
τ_w	Wall shear stress	Pa
μ	Dynamic viscosity	$Pa \cdot s^{-1}$
ρ	Density	$kg \cdot m^{-3}$

1 Introduction

Biofouling consists of the accumulation of microorganisms over surfaces and its formation and development is a complex chain of events including initial cell adhesion, microcolonies formation, multi-layered clusters development, and detachment [1, 2]. This set of events is highly dependent on: i) organism biology (e.g. fimbriae, flagella and other protein receptors [3]), ii) surface features and chemical nature (roughness and its affinity with the microorganism [2, 4]), iii) surrounding conditions (e.g. temperature, pH, nutrients [2]) and iv) flow characteristics (e.g. shear stress along the surface length [5]).

In the last years, an effort to understand this complex interdependency at the microscale has been made, with particular emphasis on microfluidic devices [6-12], which are commonly used in biomedical instrumentation (catheters, syringes, biosensors among others). In these devices, the formation of a microbial biofilm can originate serious problems to the patient health (e.g. urinary and catheter-related bloodstream infections [13, 14], implant failure [15]), beyond this, it can also compromise the lifespan of the device. The first stage, i.e., initial cell adhesion, has a huge impact on biofouling development, and therefore its understating is crucial and can lead to new and improved engineering solutions in the biomedical field.

Technological advances in biomedical instrumentation have conducted to increasingly efficient microdevices such as Cell Processing Systems, Micro-Electro-Mechanical Systems (MEMS), Lab on Chip Devices (LOC) and Point of Care Systems (POC), that often require complex geometries [16-22]. However, these complex geometries and the associated flow variations increase the probability and the available area for bacterial attachment. When this happens, the performance of the device can be at stake, particularly in geometries with narrow regions such as in cell trapping [18, 19] and cell processing systems that are used in a continuous mode like cytometry systems [16].

Localized fouling in devices with constrictions is a topic of recent research [6, 23]. When a device has headers that connect the microchannels, several behaviours are observed [5, 23] including: i) high and uniform fouling in the headers; ii) low fouling in the microchannel, and; iii) high localized fouling at the microchannel entrance. In the headers and microchannels, fouling is inversely proportional to the wall shear stresses (WSS), since when WSS increases tangential and lift forces are high enough to remove cells from the surface [24]. However, in some cases, high fouling may occur at a region of high WSS. Several explanations have been proposed for this phenomenon, including clogging by fibbers or by the so-called bridge effect [25]. Another hypothesis is that cell transport is significantly affected by the Brownian motion of the cells [6, 23, 24]. Cell diffusion occurs due to the cell concentration gradient between the bulk liquid and the wall [5, 24]. If it is assumed that cells arriving at the surface are instantaneously immobilized (perfect-sink model [24]), it is plausible that cell deposition/adhesion rates increase in regions with high local WSS, such as the microchannel entrance. In the literature, studies about the relation between the wall shear stresses and biofouling are scarce and only for simplified geometries (i.e. rectangle microchannels; [5, 12]).

Furthermore, for regions with high local WSS the role of cell diffusion on biofouling formation is not clear.

This work aim is to study the initial cell adhesion dependence on local wall shear stress in a microchannel with intercalate zones of constrictions and expansions. The cell adhesion tests were conducted in hydrodynamic conditions mimicking regions of the human body and biomedical devices, operating in steady-state. The focus was put in the cells that adhere to the bottom wall of the microchannel and the adhesion rate was studied for each zone of the channel. To support the analyses, the flow patterns were obtained by flow simulation. Additionally, to understand the role of mass transfer, the cell transport was modelled considering Brownian diffusion, sedimentation and convection. The mechanism of cell wall adhesion was simulated using the perfect sink model at the wall. Then, the predicted local Sherwood numbers (associated with the cell adhesion rates) were compared with the qualitative behaviour of experimental cell adhesion data.

2 Methods

2.1 Experimental set-up and procedures

The experimental set-up and the multi-constrictions microchannel design are shown in Figure 1. The cell suspension (Section 2.1.3) is injected through a port at the top of the microchannel (inlet; Figure 1a) and driven through a long straight rectangular section (upstream zone; Figure 1b), entering a consecutive and intercalate zone of constrictions and expansions (zoom in; Figure 1c). Afterward, the suspension arrives at a final rectangular section (downstream zone) followed by an exit chamber, exiting the device through an outlet port. Both ports have a 0.44 mm diameter holes for the connection of the microchannel to tygon® tubing.

The main dimensions of the microchannel are listed in Table 1 (before and after soft lithography manufacturing). Details of the antechamber geometry are shown in the Supplementary material: Figure S1. The upstream zone has a quadrangular cross-section (100×100 μm^2) sufficiently long to ensure the flow development (i.e. 5000 μm), as demonstrated by computational fluid dynamics (CFD). The constrictions have nominal cross-sections areas of 10×100 μm^2 while the expansions have 100×100 μm^2. The

nominal length of each constriction and expansion is 100 μm; short lengths to ensure undeveloped concentration boundary layers. Downstream, there is a long channel with 100×100 μm^2 of nominal cross-section area.

{Insert Figure 1 around here}

Table 1. Microchannel dimensions before and after soft lithography zones: antechamber, upstream, constrictions, expansions, downstream, exit chamber and inlet/outlet ports (Figure 1)

TOTAL NUMBER REPETITION ZONES	MICROCHANNEL ZONE	WIDTH / HEIGHT / LENGTH	DIMENSIONS BEFORE LITHOGRAPHY [μm]	DIMENSIONS AFTER LITHOGRAPHY [μm]
1	Antechamber	-	Figure S1a	-
1	Exit chamber	-	Figure S1b	-
1	Upstream	Width	100	80.80
		Height	100	94.4
		Length	5000	5000.0
23	Constriction	Width	10	9.3
		Height	100	94.4
		Length	100	98.7
22	Expansion	Width	100	80.8
		Height	100	94.4
		Length	100	83.5
1	Downstream	Width	100	80.8
		Height	100	94.4
		Length	9900	9566.9
1	Inlet port	Diameter	440	440
1	Outlet port	Diameter	440	440

2.1.1 Microchannel manufacture

The microchannel geometry was designed with the help of computer-aided design (CAD) software. Su-8 molds based on the designs were produced by an external supplier using chrome masks to imprint the design by photolithography. The microchannel was made from poly-dimethylsiloxane (PDMS) through soft lithography [26] using the SU-8 molds as templates. The microchannel was prepared with a homogenous mixture of PDMS and curing agent (Sygard 184, Dow Corning) at a ratio of 5:1. A desiccator connected to a vacuum pump was used to remove the air bubbles

formed during the PDMS mixing process. The PDMS mixture was poured over a SU-8 mold and kept in the oven for 20 minutes at 80 ºC. After curing, the PDMS microchannel was peeled off from the mold. Holes of 1 mm in diameter were punched through the PDMS replicas, at both ends of the channel, to provide inlet and outlet flow with the help of a syringe tip. The PDMS microchannel was sealed with a PDMS coated glass slide and kept in the oven for approximately 12 hours at 80 ºC. The final dimensions of the microchannel are summarized in Table 1.

2.1.2 Cell adhesion test

An *Escherichia coli* suspension was prepared (Section 2.1.3) and afterward injected into the microchannel (Figure 1) with the help of a syringe pump (Cetoni, neMESYS syringe pump), at a constant flow rate (Section 2.1.4). The test had a total duration of 1800 s. Tygon® tubing was used as the suspension carrier from the syringe to the microchannel inlet and from the microchannel outlet to the sink. Three independent trials were made.

The cell adhesion tests were carried out mimicking the *in vivo* body temperature (37 ºC), being the temperature monitored with the help of resistance temperature detectors. The focus was put on the adhesion of cells into the bottom wall of the microchannel. At the end of the test (after 1800 s), the cells in the bottom wall of the microchannel were photographed through an inverted fluorescence microscope (DMI 5000M, Leica Microsystems GmbH) with a 40× objective and the help of a high-resolution CCD camera (Leica DFC350FX, Leica Microsystems GmbH). For the upstream and downstream zones (Figure 1), images were captured for every 500 μm interval length, while for the shorter zones (i.e. constriction and expansion zones, Figure 1) images of the entire bottom area of each zone were captured. To identify and to count the number of cells that adhere to a specific section area, and remove the moving cells flowing above the wall, 10 images were captured during an interval of 5 s. A final image, obtained by averaging the 10 images, was obtained in tiff format as recorded by Leica Application Suite software. The sharper cells in the final image were the cells adhered (immobile) on the bottom, while the other cells appeared blurred since they were still moving (flowing). The total number of cells adhered (N_B) in each area zone (A_z) was then calculated (N_B/A_z).

2.1.3 Bacteria and culture conditions

E. coli JM109(DE3) was used since it had already demonstrated a good adhesion capacity in a different flow platform [5]. This strain was shown to have an adhesion behaviour similar to different clinical isolates including *E. coli* CECT 434 (ATCC 25922) [27] and has therefore been used in different works from our group where different biofilm platforms are used [28-30]. Furthermore, it has been demonstrated that *E. coli* can cause infections in the circulatory system [31] where the hydrodynamic conditions simulated in the present study can be found.

A starter culture was prepared as described by Teodosio et al. [32] and incubated overnight. A volume of 60 mL from this culture was centrifuged (for 10 min at 3202 × g) and the cells were washed twice with citrate buffer 0.05 M [33], pH 5.0. The pellet was then re-suspended and diluted in the same buffer to obtain a cell concentration of 7.6×10^7cell mL^{-1}.

2.1.4 Flow conditions

The effect of microchannel constrictions on cell adhesion was studied at 37 ºC under an average wall shear stress of 0.2 Pa, to mimic the conditions found in the human body and medical devices such as in circulatory system and endotracheal tubes [30, 34, 35]. The wall shear stress varies along the microchannel zones (e.g. upstream and downstream zones with lower values than constrictions), though to calculate the experimental flow rate (Q; equation 1) a reference wall shear stress (τ_w) must be selected. In this case, the upstream bottom wall was used as a reference, and a constant value of 0.2 Pa was chosen. A flow rate of 3.47×10^{-11} m^3/s was obtained considering the water viscosity at 37 ºC ($\mu = 6.92 \times 10^{-4}$ Pa·s) and the width (w) and height (h) of the microchannel, measured after manufacture (Table 1).

$$Q = \frac{wh^2\tau_w}{6\mu} \quad (1)$$

Equation 1 is an approximation valid when w is significantly larger than h [36]. The wall shear stress defined to calculate the flow rate will be, from now on, referred as "nominal wall shear stress". More accurate values were obtained by CFD (Section 3.2).

Due to the small dimensions of the microfluidic device, the flow regime is laminar with typical Reynolds numbers smaller than 1. For a square duct, the Reynolds number calculation is based on the fluid properties, flow rate and width and height of the microchannel:

$$\mathrm{Re} = \frac{2\rho Q}{(w+h)\mu} \quad (2)$$

where ρ and μ are the water density and the water kinematic viscosity (i.e. 993.36 kg·m $^{-3}$ and 6.97 × 10 $^{-7}$ m^2·s $^{-1}$ at 37 ºC respectively). A Reynolds number of 0.57 was obtained through equation 2.

2.2 Numerical simulation of cell adhesion

2.2.1 Model assumptions and equations

A numerical study was conducted considering the 3D geometry of the microchannel antechamber, the straight zones (i.e. upstream and downstream) and the constriction and expansion regions (Figure 1b; features in Table 1). The numerical domain neglects the sharper regions of the antechamber geometry (Supplementary data: Figure S1a). To model the cell transport, an Eulerian approach was used [4], which is often applied to simulate the transport of small particles in aqueous solutions. The following simplifications were assumed to model cell mass transport:

i) colloidal forces were neglected;

ii) no blocking;

iii) detachment was assumed negligible;

iv) no-slip between the cells and the fluid.

Hence, the following equation was used to simulate the cell transport by convection (first term of the equation), diffusion and sedimentation (second and third terms) in steady-state conditions.

$$\nabla\,(\vec{u}\cdot C) + \nabla(-D_{\mathrm{f}}\cdot\nabla C) + \nabla\left(\frac{\mathrm{D}_f\cdot\vec{F}_{\mathrm{G}}}{k\cdot T}\cdot C\right) = 0 \quad (3)$$

where C, $\vec{u}$, D_f, $\vec{F}_G$, k and T are respectively the cell concentration, velocity vector, Brownian diffusivity of the cells, sedimentation force, Boltzmann constant (1.38×10^{-23} $m^2 \cdot kg \cdot s^{-2} \cdot K^{-1}$) and absolute temperature.

Since the no-slip condition was assumed between the fluid and the cells, the velocity field was obtained by solving the Navier–Stokes equations and then the results were used as input values in equation 3. A D_f coefficient of cells in water of 3.6×10^{-13} $m^2 \cdot s^{-1}$ was obtained through reference [37], considering an equivalent cell diameter of 2.7 μm (the cells were assumed to have a cylindrical shape, length and diameter of 4.2 and 1.8 μm, respectively) and a density of 1085 $kg \cdot m^{-3}$ [38].

The sedimentation force was calculated by equation 4 and the corresponding velocity by equation 5.

$$\vec{F}_G = \frac{4}{3}\pi\, r_p^3\, \vec{g}\, (\rho_{cell} - \rho_w) \tag{4}$$

$$\vec{u}_G = \frac{D_f \cdot \vec{F}_G}{k \cdot T} \tag{5}$$

The substitution of equation 5 in 3, simplifies the convective diffusion equation to a more convenient form for simulation:

$$\nabla\{(\vec{u} + \vec{u}_G) \cdot C\} + \nabla(-D_f \cdot \nabla C) = 0 \tag{6}$$

Equation 6 was solved and the respective results used to analyse the cell adhesion rate in the microchannel walls as explained in the following section. To quantify the sedimentation effect on the adhesion predictions, a new set of simulations were run neglecting $\vec{u}_G$ term of equation 6.

2.2.2 Boundary conditions and numerical procedures

Numerical simulations were performed in OpenFOAM 5.0. The microchannel geometry was built in OpenSCAD 2015.03-2 and its domain was discretized into grids by cfMesh. Results in the laminar regime were obtained by solving the Navier–Stokes equations. The no-slip condition was considered for all the walls and a uniform velocity was

considered at the inlet of the microchannel antechamber. To solve the fluid flow, an adaptation of the *icoFoam* solver was used (i.e. a new adaptive time-step feature was implemented) and the velocity–pressure coupled equations were solved by PIMPLE algorithm. The numerical schemes used for the gradient, divergence and Laplacian terms of the Navier-Stokes equations were: Gauss linear, Gauss upwind and Gauss linear corrected, respectively. Simulations were made in transient mode, to assure convergence. In the numerical procedure, an adaptive time-step was considered (function of a maximum Courant number of 0.05) and an initial time-step of 10^{-10} s was set.

To solve the cell transport equation 6, the *scalarTransportFoam* solver was adapted by implementing an adaptative time-step feature. A uniform concentration of 0.35 kg·m $^{-3}$ was considered at the antechamber inlet and at the bottom walls, the cell concentration was set to zero since it is assumed that all the cells that arrive at the wall stay instantaneously immobilized and therefore disappear from the dispersed phase. This is the so-called perfect sink model, and it is the most commonly used boundary condition at the collectors surface [24, 39, 40]. In these wall conditions (i.e. of null concentration and velocity), the cell flux (J_{cell}) was calculated by:

$$J_{cell} = -D_f \cdot \nabla C \tag{7}$$

This cell flux is usually expressed in terms of the Sherwood number, which represents the ratio of the convective mass transfer to the rate of diffusive mass transport and can be calculated by [24]:

$$\mathrm{Sh} = \frac{k_m}{D_f} \cdot h \tag{8}$$

where k_m is the convective mass transfer coefficient (equation 9) and h the microchannel height.

$$k_m = \frac{J_{cell}}{(C_{bulk} - C_{wall})} \tag{9}$$

Theoretically, the number of adhered cells per area (N_B/A_z) is directly related to the cell flux (equation 7) and, consequently, to the experimental Sherwood number [39]:

$$\mathrm{Sh}_{\mathrm{exp}} = \frac{(N_B/A_Z)}{\Delta t} \cdot \frac{1}{n_\infty} \cdot \frac{h}{D_f} \tag{10}$$

where Δt is the adhesion time and n_∞ is the concentration of cells at the inlet (in cells·m^{-3}). In this work, we analyzed the correlation between Sherwood number and cell adhesion rate by comparison of the predicted Sherwood number with the experimental one (equations 8 and 10, respectively).

The numerical schemes used for the gradient, divergence and Laplacian terms of the cells transport equation were: Gauss linear, bounded Gauss upwind and Gauss linear corrected, respectively. A Gauss linear scheme was used for interpolation. The concentration equation was solved by PBiCGStab solver and the preconditioner DILU for a solution tolerance of 10^{-12}.

An extremely refined mesh was used to solve the transport cell equation (equation 6), as required to accurately represent the developing concentration boundary layer. For instance, smaller elements were placed near the bottom walls with different levels of refinement: height ranged between 0.2 and 1 μm and the length and width were 1 μm (Supplementary material: Figure S2). Mesh independence tests were conducted to ensure grid-independence results. A maximum number of mesh elements of ~700 000 per 500 μm of the microchannel length were used to solve the fluid flow and mass transport equations. Comparing the results of the most refined 2 grids (coarser mesh with ~630 000 per 500 μm of the microchannel length), mass imbalances were below 0.02 % and the maximum error of the local Sherwood number was below 2.5 %. To diminish the computer memory required per simulation, the domain was divided into 12 subdomains along the microchannel length. The solution of each subdomain was obtained in sequence (i.e. the outlet solution of subdomain 1 was the inlet solution of subdomain 2, and so on).

3 Results and discussion

3.1 Adhesion results: experimental

The total number of cells adhered to the bottom walls of the microchannel was analyzed after 1800 s of experimental time. The average values were obtained for each microchannel zone (i.e. upstream zone, constrictions, expansions and downstream zone) and divided by the corresponding zone area (upstream and downstream zones were subdivided into small sections; details in section 2.1.2). These adhesion results are shown in Figure 2 along the microchannel length.

{Insert Figure 2 around here}

Figure 2 shows that along the microchannel length, the number of cells adhered per area is approximately 8×10^5 cells·cm^{-2} along the upstream and downstream zones (square symbols). The constrictions show the highest values of cell adhesion rate while the expansions show the lowest values by comparison to upstream and downstream zones. Along the constriction zones (filled circles; Figure 2), the adhesion is 3 times higher than in the upstream and downstream zones (square symbols, Figure 2) and it is 10 times higher than in the expansion zones (unfilled circles; Figure 2). The results obtained in the multiple constrictions region show a systematic oscillation between the results of each constriction zone (filled circles; Figure 2) and each expansion zone (unfilled circles; Figure 2). Figure 3 demonstrates that the typical cell density is higher in the constrictions. It is also observed, in the expansion zones, that the percentage of the area without adhered cells is significant when compared with the constriction zones.

{Insert Figure 3 around here}

3.2 Flow characterization: numerical

To understand the initial cell adhesion dependence on local flow patterns, Figure 4 shows the velocity field in the middle *x*,*y* plane (*x*, *y*, 0), the wall shear stress in the

bottom *x*,*y* plane (*x*, *y*, -47.2 μm) and the streamlines in the middle *x*,*y* plane (*x*, *y*, 0) obtained for the inlet and the first 4 constrictions and 4 expansions of the microchannel. Similar results were obtained in the other zones of the microchannel (not shown). Higher velocities are obtained along the constrictions, while very low velocities are determined for the expansions, as expected (Figure 4a). The average wall shear stress along the bottom (weighted by area) increases from 0.27 Pa at the upstream zone to 9.4 Pa at the constrictions and decreases to 0.33 Pa at the expansions (Figure 4b). The streamlines do not show any recirculation in the expansion zones (Figure 4c).

{Insert Figure 4 around here}

Figure 5 shows the velocity profiles obtained along the upstream zone, first constriction and first expansion in the middle *z*,*x* plane (*x*, 0, *z*). The velocity profile is fully developed along the upstream zone (l_2, Figure 5), attaining a maximum velocity of 7.5×10^{-3} m/s (in the figure, the velocity profiles are normalized by this maximum value in the upstream zone). Along the constriction, the velocity is 5 to 6 times higher than in the upstream zone (l_3 to l_5; Figure 5), while in the expansion centerline, the velocity tends to the value observed in the upstream zone (at l_6). There is good agreement between the profiles obtained at the entrance and at the exit of the contractions. Furthermore, it is also clear a considerable reduction of the boundary layer in zones with high velocity. This is consistent with the significant rise of the local wall shear stress shown in Figure 4b.

{Insert Figure 5 around here}

3.3 Mass transport: numerical

The cell concentration in the vicinity of the bottom wall is shown in Figure 6. The concentration maps were obtained along the middle *x*,*z*-plane of the microchannel (*x*,0,*z*) in the upstream zone (Figure 6a), in the constrictions/expansions zone (Figure 6b) and in the downstream zone (Figure 6c). At the antechamber, the concentration

boundary layer starts developing and it continues along the upstream zone of the microchannel. For instance, at *x*-lengths 25 and 4500 μm, the layer thickness increases from ~2.5 to ~13.2 μm (Figure 6a and b). As the suspension enters the first constriction (Figure 6b), the concentration boundary layer first decreases and then increases until the end of the constriction (maximum of 9.2 μm). Through the expansion zone, the concentration boundary layer increases to a maximum of 12.0 μm and then decreases until the next inlet zone. Between the first and last constrictions, the thickness of the boundary layer decreases and, in the downstream zone, reaches a minimum of 1.4 μm (Figure 6c).

To understand the role of convection and Brownian diffusion on cell adhesion, the average Sherwood number obtained for each microchannel zone is shown in Figure 7 (i.e. upstream zone, constrictions, expansions and downstream zone). The predicted Sherwood number increases along the first 3500 μm of the upstream zone (blue squares; Figure 7) from 11.5 to 19.4, however, after this location, the Sherwood number stays approximately constant. Only, at the end of the upstream zone and just before the first constriction, a sudden increase is observed (Sh = 27.5); a similar tendency is observed in the experimental results (black series; Figure 7). Comparing the predicted Sherwood number of the entire microchannel zones (upstream zone, constrictions, expansions and downstream zone; Figure 7), the constrictions show the highest Sherwood values while the upstream and downstream zones show the lowest values. The numerical Sherwood number in the constriction zones (blue filled circles; Figure 7) is ~13 times higher than in the upstream zone (blue square symbols; Figure 7) and it is 6 times higher than in the expansion zones (blue unfilled circles; Figure 7). Along the downstream zone, the predicted Sherwood number decreases significantly from 72.7 to 26.6. The experimental Sherwood number obtained for each microchannel zone (black series; Figure 7) is directly related to the adhesion behaviour (equation 10), and for that reason Figures 7 and 2 show the same tendency. An overall analysis of Figure 7 indicates that the numerical predictions of Sherwood number obtained for the expansion and constriction zones are above the predictions for the upstream and downstream zones, while the experimental Sherwood number for the expansion zones is below the experimental results for the upstream and downstream zones. Besides, the predicted Sherwood curve along the downstream region shows a different slope relatively to the experimental one.

In regions with low Sherwood numbers, such as in the upstream and downstream zones, the sedimentation has a significant role in cell adhesion contributing to 26 % of the predicted Sherwood number, i.e. $100 \times (\mathrm{Sh}_{\text{with gravity}}\text{-}\mathrm{Sh}_{\text{without gravity}})/\mathrm{Sh}_{\text{with gravity}} = 0.26$. In the constriction and expansion zones, the Sherwood number is affected between 4 to 7 percentage points by the sedimentation.

{Insert Figure 6 around here}

{Insert Figure 7 around here}

A qualitative comparison between the predicted map of Sherwood number with the experimental data of cells adhered to the bottom wall is shown in Figure 8. Figure 8 demonstrates that cell adhesion mainly occurs at the inlet and along the central region of the constrictions, with Sherwood numbers ranging between 85 and 260. A similar distribution of Sherwood number is obtained in the remaining constriction zones (Supplementary material: Figure S3). The distribution of the numeric Sherwood number is truly non-uniform in the expansion zones, having local maximum values at opening/exit regions (~ 300) and low values in a high percentage of the area (~ 2). Further, the maximum Sherwood values are obtained near the constriction walls.

{Insert Figure 8 around here}

4 Discussion

The experimental cell adhesion data obtained for the upstream and downstream zones (square symbols, Figure 2) can be clearly understood by analysing the flow patterns (Figure 4a). The cell suspension flows through the rectangular and long upstream section, which is sufficiently long to ensure a developed flow (Figure 5). The hydrodynamic conditions acting on the cells are, for that reason, constant through

almost this zone entire length, and so the cell adhesion is approximately constant along this zone. When the suspension enters the first constriction, the flow area decreases 10-fold (Table 1), and consequently, the fluid velocity increases significantly (i.e. ~6-fold increase in the maximum velocity; Figure 4a). Due to the increase of wall shear stress, which leads to the increase of drag and lift forces over the cells [41], cell adhesion would be expected to decrease, a phenomenon already observed in straight channels [31]. However, the results show an opposite tendency (unfilled circles; Figure 2), highlighting the contribution of convection and Brownian diffusion mechanisms to cell transport. The tangential velocity is higher in the constrictions (Figure 5), increasing the mass transport by convection and decreasing the thickness of the mass boundary layer (Figure 6), implying a higher cell concentration gradient and a high rate of cells reaching the wall. For that reason, adhesion increases in locations with sudden increase in shear rate, such as constrictions. This behaviour supports our unconventional results (filled circles; Figure 2) and the numerical predictions shown in sections 3.2 and 3.3 confirm this hypothesis.

At the end of the upstream zone (Figure 6b), the concentration boundary layer is still developing, and when the first constriction starts, the fluid velocity increases and the thickness of the concentration boundary layer decreases (Figure 6b). Furthermore, the constriction is short and so the concentration boundary layer is still developing at the end of the constriction (entrance of the expansion; Figure 6b). As a consequence, the thickness of the boundary layer along the constriction is always smaller than in the upstream zone (maximum deviation of ~4.0 μm; Figure 6a), resulting in high Sherwood numbers (inversely proportional to boundary layer thickness; Figure 7) and high adhesion values. The expansion zones have a short length and, consequently, a developing concentration boundary layer (Figure 6b), but at the same time, the experimental data shows the lowest values of adhered cells per area (unfilled circles; Figure 2). Low adhesion is correlated to low Sherwood number in these regions, as the Sherwood number in the expansions is lower than in the constrictions.

An interesting similarity between experimental and predicted local Sherwood data evolution along the microchannel is shown in Figure 7, particularly in the upstream and constriction zones. This promising behaviour is reinforced by the correlation between adhered cells and local Sherwood distribution demonstrated in Figure 8. This

correlation suggests that local Sherwood numerical predictions may be a way to identify and correct possible blocking zones, even before the construction of the prototype.

Nevertheless, quantitatively, the predicted Sherwood numbers are systematically higher than the experimental data (Figure 7), respectively, 1.2 and 3.5 times in the upstream and constriction zones (squares and filled circles). The comparison between predicted and experimental Sherwood data in the expansion zones (filled circles; Figure 7) shows that the physical model proposed to predict cell adhesion (equation 6) is not sufficiently accurate and additional factors need to be considered: colloidal forces, hydrodynamics forces [33] exerted on adhered cells, the presence of surface appendages (*e.g.* flagella and pili), expression of adhesins and other biological factors [5, 42]. The perfect sink boundary condition would need to be modified to include phenomena associated to colloidal and hydrodynamic forces exerted on cells, such as blocking and detachment.

5 Conclusions

An experimental cell adhesion test was conducted for the first time in a microchannel with multiple constrictions, for operating conditions obtained in biomedical devices. An unexpected increase in cell adhesion was obtained in regions where the local wall shear stress was high, as in constrictions. The multiple constrictions showed an increase of local cell adhesion when compared to long and straight microchannel zones, with lower local wall shear stress. This probably occurred because, for this flow regime, the convection and diffusion mechanisms have a relevant impact on the transport of cells. This impact was assessed indirectly by numerical analysis. The comparison of numerical and experimental data of cell adhesion showed the same tendency and highlighted the importance of mass transport.

Our study provides a new explanation for the increase of the fouling in the microchannels entrance and narrow regions of microdevices. Furthermore, the described numerical approach can be used to analyse several opposing requirements and to correlate the obtained wall shear stress with the number of adhered cells (Sherwood number), as a way to identify possible blocking zones and defining solutions, even before the construction of the prototype.

Credit author statement

S. F. Neves: Methodology, Investigation, Writing –Original Draft, Writing - Review & Editing, Software, Data Curation, Visualization

J. Ponmozhi: Investigation, Writing –Original Draft, Data Curation

F. J. Mergulhão: Conceptualization, Resources, Writing - Review & Editing, Methodology, Supervision, Funding acquisition

J. B. L. M. Campos: Resources, Writing - Review & Editing, Supervision, Project administration, Funding acquisition

J. M. Miranda: Conceptualization, Methodology, Software, Visualization, Writing – Original Draft, Writing - Review & Editing, Supervision, Project administration, Funding acquisition

Declaration of interests

x The authors declare that they have no known competing financial interests or personal relationships that could have appeared to influence the work reported in this paper.

Acknowledgments

This work was partially supported by National Funds through FCT- Foundation for Science and Technology under the projects: PTDC/EQU-FTT/105535/2008 and PTDC/QEQ-FTT/4287/2014 - POCI-01-0145-FEDER-016861. This work was also supported by base Funding - UIDB/00532/2020 of the Transport Phenomena Research Center – CEFT and UIDB/00511/2020 of the Laboratory for Process Engineering, Environment, Biotechnology and Energy – LEPABE - funded by national funds through the FCT/MCTES (PIDDAC).

The cell images shown in the Graphical abstract were adapted from: https://smart.servier.com/smart_image/bacterium-2/; the image is licensed under a Public Creative Commons Attribution 3.0 Unported License.

References

1. Unosson, E., *Antibacterial Strategies for Titanium Biomaterials*. 2015. p. 19.
2. Garrett, T.R., M. Bhakoo, and Z. Zhang, *Bacterial adhesion and biofilms on surfaces.* Progress in Natural Science, 2008. **18**(9): p. 1049-1056.
3. Dalton, H.M. and P.E. March, *Molecular genetics of bacterial attachment and biofouling.* Current Opinion in Biotechnology, 1998. **9**(3): p. 252-255.
4. Carniello, V., et al., *Physico-chemistry from initial bacterial adhesion to surface-programmed biofilm growth.* Advances in Colloid and Interface Science, 2018. **261**: p. 1-14.
5. Moreira, J.M., et al., *The effects of surface properties on Escherichia coli adhesion are modulated by shear stress.* Colloids Surf B Biointerfaces, 2014. **123**: p. 1-7.
6. Schoenitz, M., et al., *Fouling in microstructured devices: a review.* Chemical Communications, 2015. **51**(39): p. 8213-8228.
7. Meyer, M.T., et al., *Development and validation of a microfluidic reactor for biofilm monitoring via optical methods.* Journal of Micromechanics and Microengineering, 2011. **21**(5): p. 054023.
8. Valiei, A., et al., *A web of streamers: biofilm formation in a porous microfluidic device.* Lab on a Chip, 2012. **12**(24): p. 5133-5137.
9. Rusconi, R., et al., *Laminar flow around corners triggers the formation of biofilm streamers.* Journal of The Royal Society Interface, 2010. **7**(50): p. 1293-1299.
10. Kim, K.P., et al., *In situ monitoring of antibiotic susceptibility of bacterial biofilms in a microfluidic device.* Lab on a Chip, 2010. **10**(23): p. 3296-3299.
11. Zhang, Z.L., et al., *In situ bio-functionalization and cell adhesion in microfluidic devices.* Microelectronic Engineering, 2005. **78–79**(0): p. 556-562.
12. Salek, M.M., S.M. Jones, and R.J. Martinuzzi, *The influence of flow cell geometry related shear stresses on the distribution, structure and susceptibility of Pseudomonas aeruginosa 01 biofilms.* Biofouling, 2009. **25**(8): p. 711-725.
13. Ramstedt, M., et al., *Evaluating Efficacy of Antimicrobial and Antifouling Materials for Urinary Tract Medical Devices: Challenges and Recommendations.* Macromol Biosci, 2019. **19**(5): p. e1800384.
14. Ikram, S., et al., *Bacillus cereus biofilm formation on central venous catheters of hospitalised cardiac patients.* Biofouling, 2019. **35**(2): p. 204-216.
15. Orapiriyakul, W., et al., *Antibacterial surface modification of titanium implants in orthopaedics.* Journal of Tissue Engineering, 2018. **9**: p. 2041731418789838.
16. Huh, D., et al., *Microfluidics for flow cytometric analysis of cells and particles.* Physiol Meas, 2005. **26**(3): p. R73-98.
17. Sollier, E., et al., *Fast and continuous plasma extraction from whole human blood based on expanding cell-free layer devices.* Biomedical Microdevices, 2010. **12**(3): p. 485-497.
18. Tan, W.-H. and S. Takeuchi, *A trap-and-release integrated microfluidic system for dynamic microarray applications.* Proceedings of the National Academy of Sciences, 2007. **104**(4): p. 1146-1151.
19. Zhang, Q., et al., *Microbial detection in microfluidic devices through dual staining of quantum dots-labeled immunoassay and RNA hybridization.* Analytica Chimica Acta, 2006. **556**(1): p. 171-177.
20. Bento, D., et al., *Microbubble moving in blood flow in microchannels: effect on the cell-free layer and cell local concentration.* Biomedical Devices, 2016.
21. Hou, H.W., et al., *A microfluidics approach towards high-throughput pathogen removal from blood using margination.* Biomicrofluidics, 2012. **6**(2): p. 024115.
22. Sha, J., et al., *Capillary-composited microfluidic device for heat shock transformation of Escherichia coli.* Journal of bioscience and bioengineering, 2011. **112**(4): p. 373-378.
23. Huber, D., et al., *Hydrodynamics in Cell Studies.* Chem Rev, 2018. **118**(4): p. 2042-2079.

24. Elimelech, M., *Particle Deposition on Ideal Collectors from Dilute Flowing Suspensions - Mathematical Formulation, Numerical-Solution, and Simulations.* Separations Technology, 1994. **4**(4): p. 186-212.
25. Hartman, R.L., *Managing Solids in Microreactors for the Upstream Continuous Processing of Fine Chemicals.* Organic Process Research & Development, 2012. **16**(5): p. 870-887.
26. Xia, Y. and G.M. Whitesides, *Soft Lithography.* Annual Review of Materials Science, 1998. **28**: p. 153-184.
27. Gomes, L.C., et al., *96-well microtiter plates for biofouling simulation in biomedical settings.* Biofouling, 2014. **30**(5): p. 535-46.
28. Alves, P., et al., *The potential advantages of using a poly(HPMA) brush in urinary catheters: effects on biofilm cells and architecture.* Colloids Surf B Biointerfaces, 2020. **191**: p. 110976.
29. Moreira, J.M.R., et al., *Micro- and macro-flow systems to study Escherichia coli adhesion to biomedical materials.* Chemical Engineering Science, 2015. **126**: p. 440-445.
30. Lopez-Mila, B., et al., *Effect of shear stress on the reduction of bacterial adhesion to antifouling polymers.* Bioinspir Biomim, 2018. **13**(6): p. 065001.
31. Micol, R., et al., *Escherichia coli native valve endocarditis.* Clin Microbiol Infect, 2006. **12**(5): p. 401-3.
32. Teodosio, J.S., et al., *Flow cell hydrodynamics and their effects on E. coli biofilm formation under different nutrient conditions and turbulent flow.* Biofouling, 2011. **27**(1): p. 1-11.
33. Simoes, M., et al., *The effects of a biocide and a surfactant on the detachment of Pseudomonas fluorescens from glass surfaces.* Int J Food Microbiol, 2008. **121**(3): p. 335-41.
34. Muller, W.J., S. Gerjarusek, and P.W. Scherer, *Studies of wall shear and mass transfer in a large scale model of neonatal high-frequency jet ventilation.* Ann Biomed Eng, 1990. **18**(1): p. 69-88.
35. Fan, R., et al., *Circulatory shear flow alters the viability and proliferation of circulating colon cancer cells.* Sci Rep, 2016. **6**: p. 27073.
36. Busscher, H.J. and H.C. van der Mei, *Microbial adhesion in flow displacement systems.* Clinical microbiology reviews, 2006. **19**(1): p. 127-141.
37. Li, A. and G. Ahmadi, *Dispersion and Deposition of Spherical Particles from Point Sources in a Turbulent Channel Flow.* Aerosol Science and Technology, 1992. **16**(4): p. 209-226.
38. Kubitschek, H.E., W.W. Baldwin, and R. Graetzer, *Buoyant density constancy during the cell cycle of Escherichia coli.* Journal of Bacteriology, 1983. **155**(3): p. 1027-1032.
39. Jin, C., et al., *Non-linear, non-monotonic effect of nano-scale roughness on particle deposition in absence of an energy barrier: Experiments and modeling.* Scientific Reports, 2015. **5**: p. 17747.
40. Unni, H.N. and C. Yang, *Kinetics of Colloidal Particle Deposition to a Solid Surface from Pressure Driven Microchannel Flows.* The Canadian Journal of Chemical Engineering, 2007. **85**(5): p. 609-616.
41. Boulbene, B., et al., *A combined computational fluid dynamics (CFD) and experimental approach to quantify the adhesion force of bacterial cells attached to a plane surface.* AIChE journal, 2012. **58**(12): p. 3614-3624.
42. Kimkes, T.E.P. and M. Heinemann, *How bacteria recognise and respond to surface contact.* FEMS Microbiol Rev, 2020. **44**(1): p. 106-122.

Caption for figures

Figure 1. Schematic of (not to scale): a) experimental set-up, b) microchannel (inlet/outlet ports, antechamber, upstream, multiconstrictions, downstream and exit chamber) and c) multiconstrictions zoom with two constrictions and one expansion; [legend in μm: W_e = 80.8, l_e = 83.5, W_c = 9.31, l_c = 98.7 and h = 94.4]

Figure 2. Adhesion in the microchannel bottom walls for τ = 0.2 Pa and at 37 ºC; number of cells adhered per zone area along the microchannel length

Figure 3. Cells adhered in the bottom walls of the constriction and expansion zones of the microchannel

Figure 4. Zoomed view at the upstream zone and the first 4 constrictions and 4 expansions of the microchannel (in red in the microchannel illustration); a) velocity magnitude in the middle *x*,*y* plane (*x*,y,0), b) wall shear stress in the bottom plane (*x*, *y*, -47.2 μm) and c) streamlines in the middle *x*,*y* plane (*x*,*y*,0)

Figure 5. Velocity profile obtained in the middle z,*x* plane (*x*, 0, *z*) at seven positions identified in the microchannel illustration (not to scale)

Figure 6. Concentration map in three sections (AA'', BB'' and CC'') in the middle *x*,*z*-plane (x,0, z) (example of section AA'' shown in microchannel illustration)

Figure 7. Comparison of experimental (in black) and numerical (in blue) Sherwood numbers obtained for each microchannel zone (i.e. bottom of the upstream, constrictions, expansions and downstream sections)

Figure 8. A composite image combining 10 sections of the microchannel showing the local Sherwood number and the location of the cells adhered to the bottom wall.

Figure 1.tif

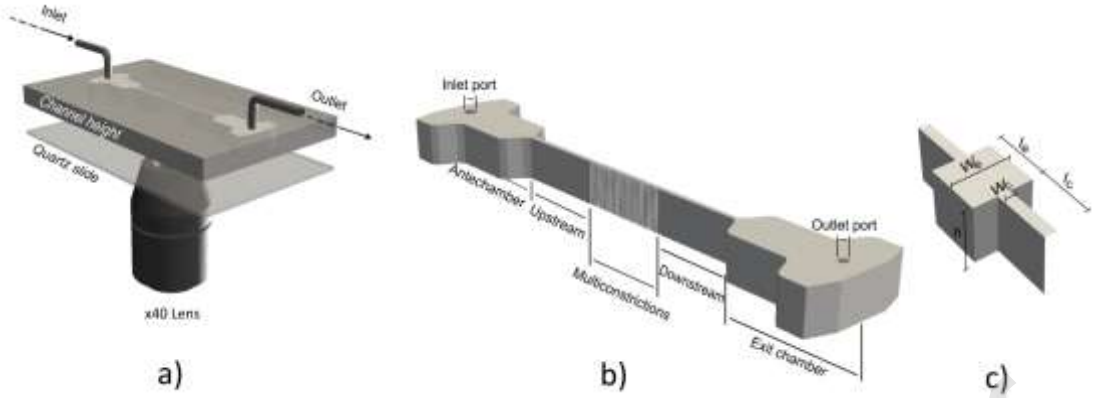

Figure 2.pdf

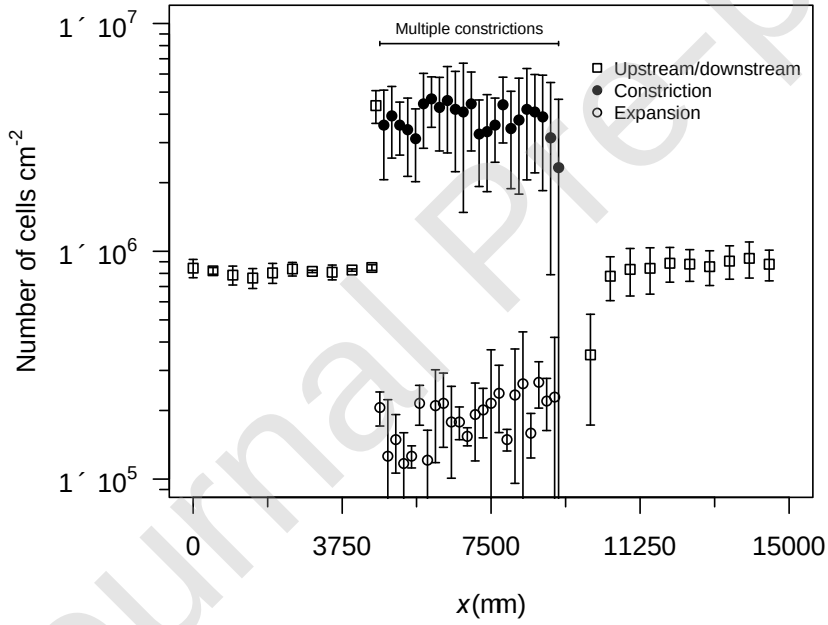

Figure 3.tif

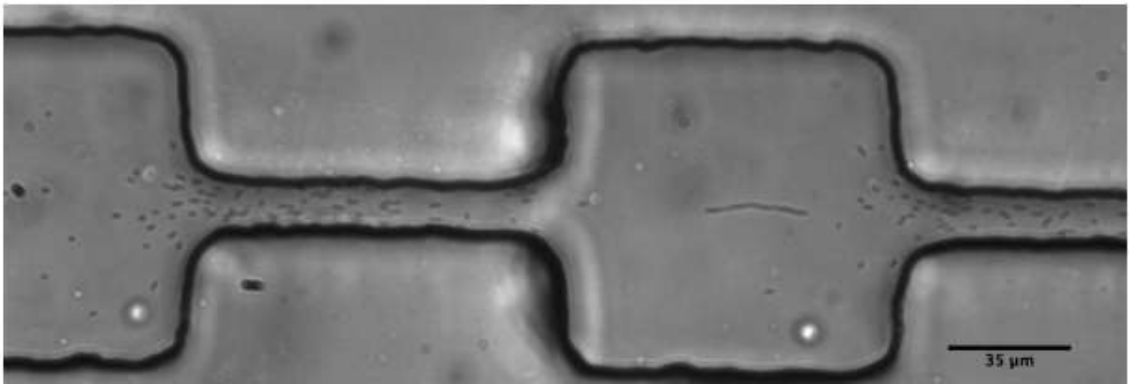

Figure 4.tif

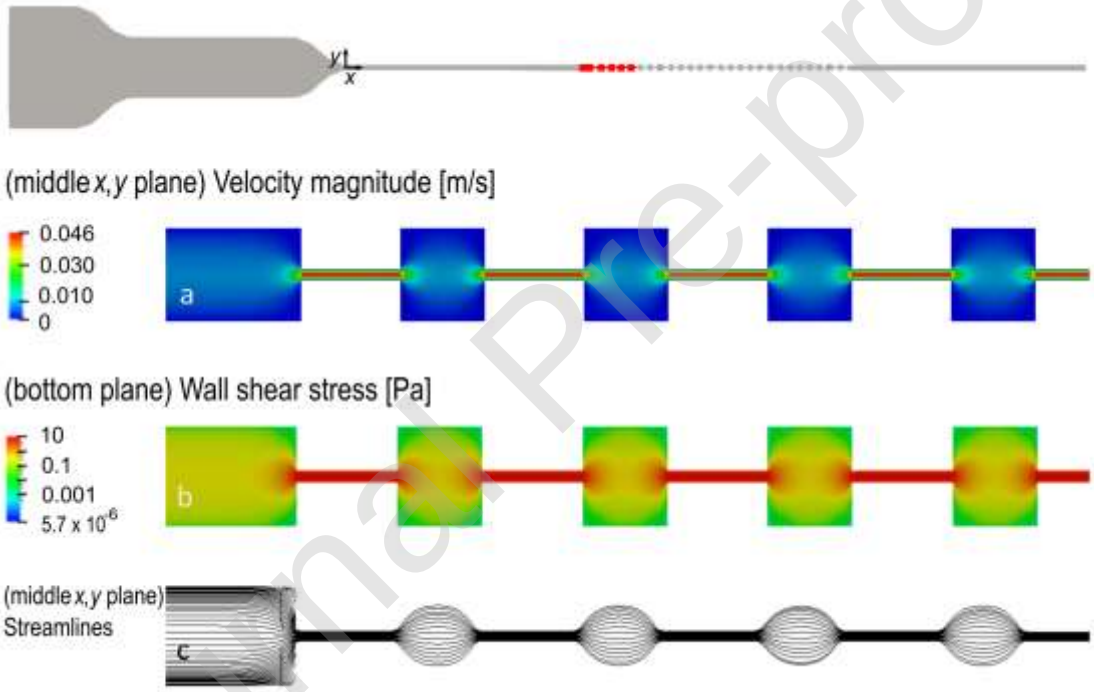

Figure 5.tif

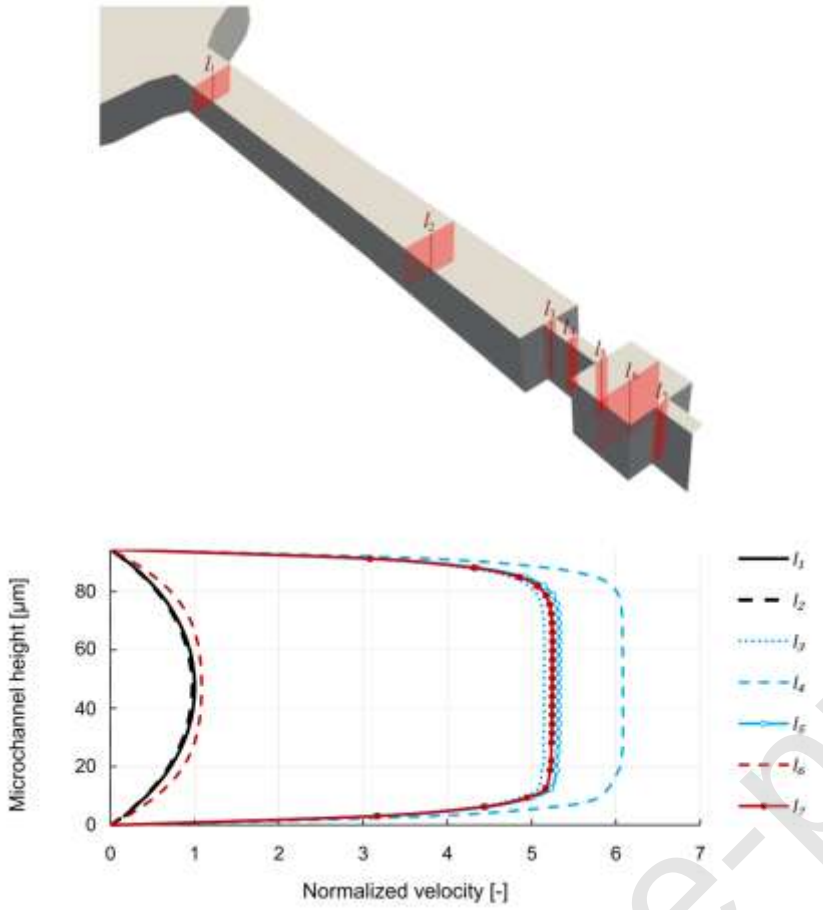

Figure 6.tif

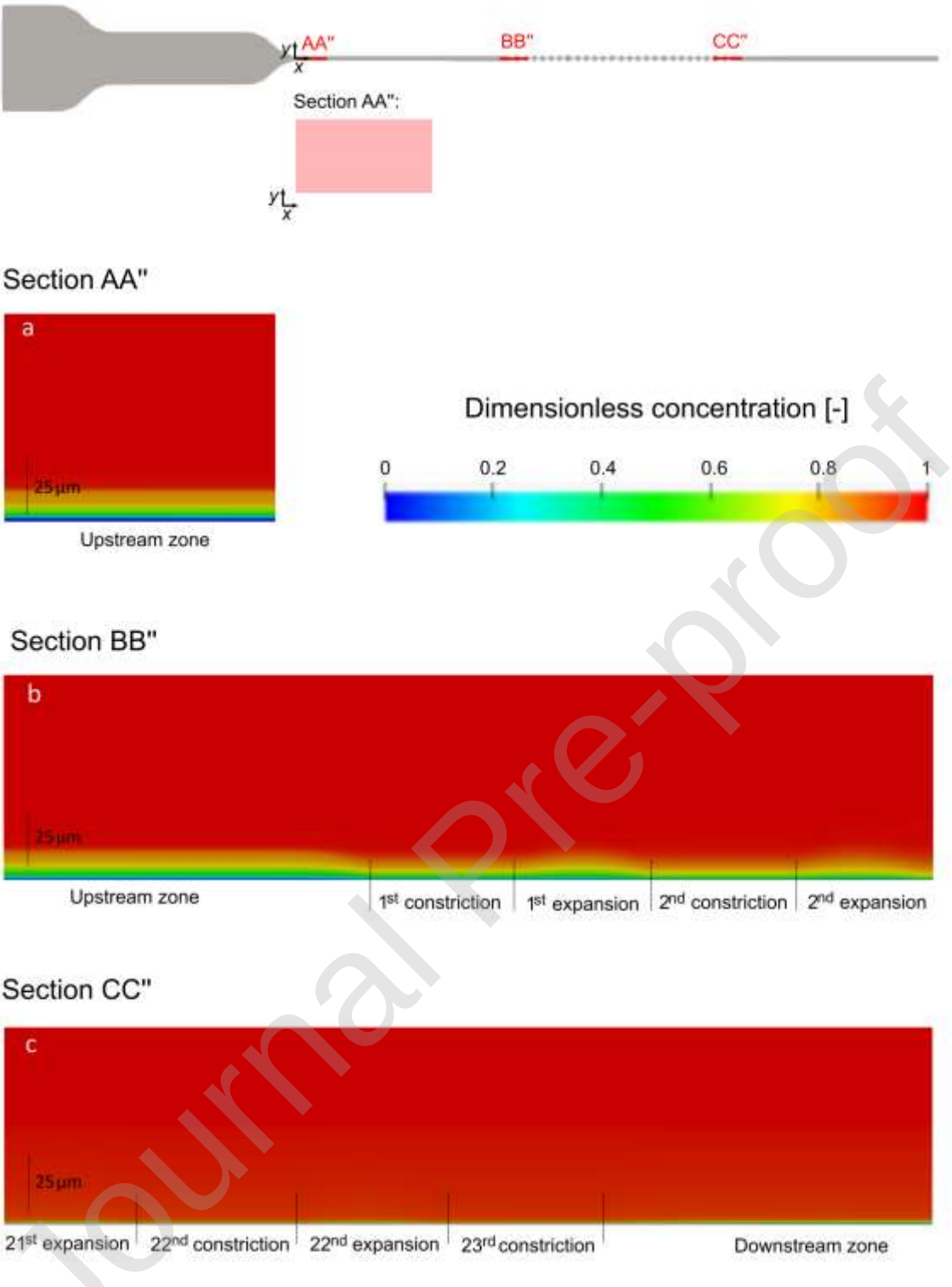

Figure 7.tif

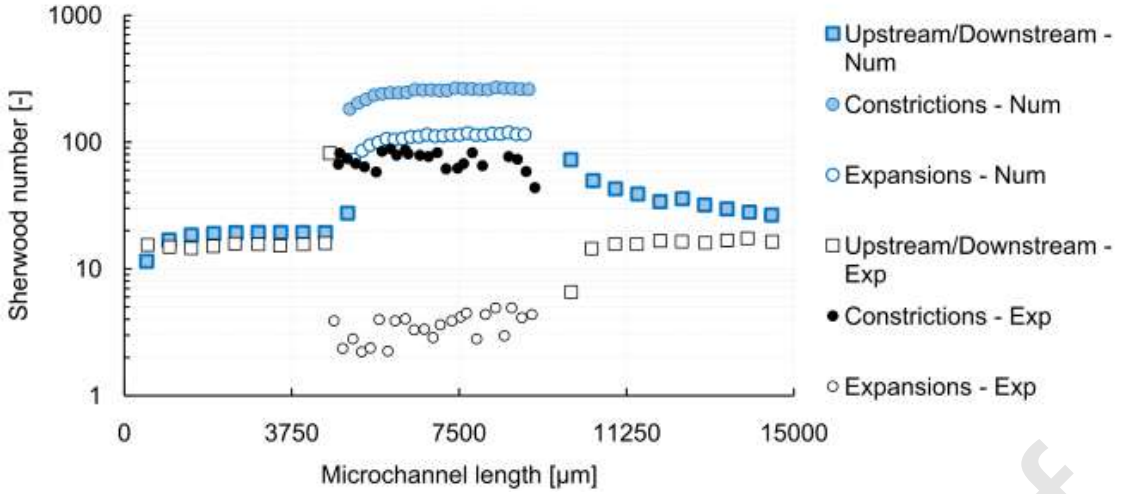

Figure 8.tif